



# UNIVERSITÀ DI PARMA

## ARCHIVIO DELLA RICERCA

University of Parma Research Repository

Cracking in autoclaved aerated concrete: Experimental investigation and XFEM modeling

This is the peer reviewed version of the following article:

*Original*

Cracking in autoclaved aerated concrete: Experimental investigation and XFEM modeling / Ferretti, Daniele; Michelini, Elena; Rosati, G.. - In: CEMENT AND CONCRETE RESEARCH. - ISSN 0008-8846. - 67:(2015), pp. 156-167. [10.1016/j.cemconres.2014.09.005]

*Availability:*

This version is available at: 11381/2765338 since: 2021-10-21T15:35:49Z

*Publisher:*

Elsevier Ltd

*Published*

DOI:10.1016/j.cemconres.2014.09.005

*Terms of use:*

Anyone can freely access the full text of works made available as "Open Access". Works made available

*Publisher copyright*

note finali coverpage

(Article begins on next page)

02 May 2026

# Cracking in autoclaved aerated concrete: experimental investigation and XFEM modeling

D. Ferretti<sup>1</sup> \*, E. Michelini<sup>1</sup> and G. Rosati<sup>2</sup>

<sup>1</sup> Department of Civil, Environmental, Land Management Engineering and Architecture, University of Parma, P.co Area delle Scienze 181/A, 43124 Parma, Italy

<sup>2</sup> Department of Civil and Environmental Engineering, Politecnico di Milano, Piazza L. Da Vinci 32, 20133 Milano, Italy

\* Corresponding author. Tel. +39 0521 905943; fax +39 0521 905924.

E-mail address: daniele.ferretti@unipr.it (D. Ferretti).

## ABSTRACT

*The paper aims to investigate and model cracking development in beams and deep-beams made of autoclaved aerated concrete (AAC). Fracture mechanics of AAC has been first studied by performing three-point bending tests on beams, similar to those commonly used for ordinary concrete elements. In some of these tests, crack growth has been also monitored by using ESPI laser technique. In this way, it has been possible to calibrate the main parameters of a proper cohesive law by means of extended finite element inverse analysis. Subsequently, cracking tests have been also performed on deep-beams, whose behavior is more representative of full scale walls. To validate the proposed cohesive law, deep-beams experimental behavior has been finally simulated through XFEM.*

## KEYWORDS

AAC; ESPI; cracking; cohesive model; XFEM.

## 30 1. INTRODUCTION

31 In recent years, autoclaved aerated concrete (AAC) has been widely recognized as  
32 a high quality, innovative material that has been extensively used for the realization of  
33 residential, commercial and industrial buildings.

34 As known, AAC is a lightweight structural material with interesting sound and  
35 thermal insulation properties, so allowing satisfying increasingly stringent building  
36 design requirements, whilst ensuring environmental compliance [1, 2]. From a structural  
37 point of view, AAC is suitable for the realization of masonry bearing walls of low-to-  
38 medium rise buildings, since it offers high fire-resistance, due to its incombustible  
39 nature, and adequate mechanical properties, at least for the material with higher density  
40 values (corresponding to higher compressive strengths). The structural behavior of AAC  
41 – especially under accidental or seismic loads – is also influenced by its toughness,  
42 which exerts an important role on its resistance against damage during transport and  
43 handling [3]. Fracture toughness is also relevant with respect to cracking, which  
44 represents a quite common problem of AAC masonry even under static loads. This  
45 problem is particularly significant for AAC internal partitions, due to the deformability  
46 of the upper floor, which can lean on them – thus representing an additional, not  
47 calculated load – or to that of the bottom floor, which can drag down the wall,  
48 connected to it.

49 The mechanical study of this problem requires the knowledge of material  
50 properties, like tensile strength and fracture energy. These latter have been mainly  
51 analyzed in the past through experimental tests on compact tension specimens and  
52 wedge-splitting specimens, whose results can be found in the technical literature [3-7].

53 Aim of this work is to investigate cracking development in AAC walls under  
54 static loads and, more generally, cracking in AAC structures. To this scope, three point  
55 bending tests, similar to those commonly used for ordinary concrete, have been  
56 performed on AAC elements, trying to overcome the difficulties related to crack  
57 propagation control. More in details, a preliminary set of tests on both AAC beams and  
58 deep-beams has been performed under loading control, so as to quantify the statistical  
59 variability of material tensile strength. Subsequently, similar specimens have been  
60 tested under crack-mouth opening displacement (*CMOD*) control, so as to obtain the

61 complete load-displacement curve and, consequently, the material fracture energy  $G_F$ .  
62 In order to determine a proper cohesive law, crack propagation has been observed by  
63 using ESPI technique (Electronic Speckle Pattern Interferometry), which allows to  
64 observe the displacement field of a surface illuminated by a laser light with a precision  
65 higher than 10  $\mu\text{m}$ . This has permitted to detect the cracking onset and to observe the  
66 crack profile. The so obtained results have been then used for calibrating the parameters  
67 of a proper cohesive law through an inverse analysis procedure, performing a non-linear  
68 extended finite element analysis; this law substantially agrees with those available in the  
69 literature, obtained through wedge-splitting tests [4]. Finally, the proposed cohesive law  
70 has been adopted in a XFEM model so as to reproduce the experimental cracking  
71 growth in a reduced scale AAC wall.

72

## 73 **2. EXPERIMENTAL TESTS ON AAC**

### 74 ***2.1 Mechanical characterization of the material***

75 As already mentioned, the first part of the experimental program aimed to provide  
76 a mechanical characterization of the investigated material, by quantifying at the same  
77 time the statistical variability of the most important properties. Before testing, all the  
78 investigated samples, characterized by an average density  $\rho \approx 550 \text{ kg/m}^3$ , were cured in  
79 laboratory conditions so as to reach relatively low moisture contents. It should be  
80 indeed reminded that AAC strength is influenced by several parameters, which are not  
81 only related to specimen size and shape, but also to method of pore formation, direction  
82 of loading, age, moisture content, characteristics of ingredients adopted in the mix, and  
83 method of curing [8, 9].

84 As known, AAC compressive strength is usually determined on cubes with an  
85 edge length of 100 mm, even if cubes with an edge length of 150 mm can be also used  
86 according to RILEM [3]; within this range the size of samples does not influence the  
87 results. In the technical literature, also cylindrical or prismatic samples are often used  
88 (e.g., [10]); in this case, the measured strength is generally lower than that determined  
89 on cubes and decreases with increasing sample slenderness (it is approximately 5%  
90 lower for slenderness equal to 2-3, [3, 11]). It is also possible to determine the  
91 compressive strength by directly testing the block units [3, 12]; the so obtained values

92 may be up to 10% lower than the ones measured on cubes. In this case, the maximum  
93 sustainable load of the unit and the corresponding compressive strength is indeed  
94 governed by the failure of the weaker side of the specimen.

95 In this paper, the statistical variability of AAC mechanical properties (strength  
96 and deformability parameters in compression) has been investigated with reference to  
97 specimens characterized by different shapes and dimensions, so as to understand if the  
98 results provided by standard tests can be used to effectively model the behavior of full-  
99 scale walls, especially in case of internal partitions. To this scope, the results obtained  
100 on "traditional" specimens, that is to say cubes with an edge length of 100 mm and  
101 prisms with slenderness equal to 2 (characterized by a 40 mm x 40 mm square basis and  
102 an height of 80 mm), have been compared with those provided by non-standard  
103 samples, represented by blocks and reduced scale walls. More in details, the attention  
104 has been focused on blocks with a loaded area equal to 625 x 100 mm and a height  
105 equal to 250 mm, commonly used for the realization of internal partitions, as well as on  
106 small AAC walls, with a loaded area equal to 625 x 100 mm and a height equal to  
107 750 mm.

108

### 109 ***2.1.1 Uniaxial compression tests on AAC blocks***

110 At first, 13 compression tests have been performed on AAC blocks for internal  
111 partitions. Before testing, all the specimens have been cured in laboratory conditions for  
112 about three months until the reaching of a moisture content lower than 10%. Tests have  
113 been carried out at the Material and Testing Laboratory of the AAC Manufacturer  
114 Company (in Piacenza, Italy), by using a Metrocom PV50 press working under loading  
115 control, with a capacity of the hydraulic actuator equal to 5000 kN and a loading rate of  
116 25 kN/min [13]. The adopted test arrangement is shown in Figure 1; in order to apply a  
117 distributed load, a 650 mm long steel rigid beam with I-section has been placed on the  
118 top of the specimen. AAC surfaces have been preliminary flattened by sandpaper to  
119 eliminate any irregularity and thereby ensure a complete contact between the specimen  
120 and the testing apparatus; furthermore, thin cardboard layers have been interposed  
121 between the specimen itself and the loading press, so as to minimize the confinement  
122 effect due to friction and apply a more uniform state of stress. Three of the 13

123 specimens have been also instrumented with linear variable displacement transducers  
124 (LVDTs, see Fig. 1), in order to measure vertical and horizontal strains,  $\varepsilon_V$  and  $\varepsilon_H$ , so as  
125 to determine the material elastic modulus  $E$  and the Poisson coefficient  $\nu$ .

126 As can be seen in Figure 2a, these tests have highlighted a small variability of  
127 compressive strength, due to the homogenous structure of the material. The average  
128 value of ultimate load was approximately equal to  $P_c = 150.5$  kN, corresponding to a  
129 nominal compressive strength  $f_c = 2.43$  MPa, with a coefficient of variation  $CV = 0.14$ .  
130 In the most of the examined cases, specimen failure was characterized by a widespread  
131 cracking, which was mainly concentrated near one of the external corners (Fig. 2b), in  
132 the weaker part of the block. As a matter of fact, because of material preparation  
133 process, the behavior in the direction of the rise of the mass during manufacturing –  
134 perpendicular to loading direction, for the analyzed specimens – is indeed variable  
135 along mould height, since the bottom part is significantly more dense and stronger than  
136 the top one [12]; as a consequence, one edge of each tested specimen was necessarily  
137 less resistant than the other, so influencing the resultant failure load. From the 3  
138 instrumented tests it has been also possible to indirectly determine both the elastic  
139 modulus and the Poisson coefficient, which were respectively equal to  $E = 1285$  MPa  
140 and  $\nu = 0.38$ , with a coefficient of variation approximately equal to 3%. More in details,  
141 the elastic modulus has been evaluated with reference to a stress interval ranging  
142 between  $0.02f_c$  and  $0.33f_c$ , according to the procedure included in RILEM  
143 Recommendations [3]. The so obtained elastic modulus appears to be quite in  
144 agreement with the results provided by other experimental campaigns available in the  
145 literature [11,14], as well as with the value derivable from a semi-empirical relation  
146 between the elastic modulus  $E$  and the compressive strength  $f_c$  suggested in [11,14]. By  
147 substituting the experimental value of compressive strength,  $f_c = 2.43$  MPa, in this  
148 expression, which is here reported for reading convenience (with  $f_c$  and  $E$  in psi):

$$149 \quad E = 6500 f_c^{0.6} \quad (1)$$

150 a value of  $E = 1512$  MPa can be obtained, which is about 15% higher than the measured  
151 one. The same Authors [11,14] also indicates that the modulus of elasticity tested  
152 parallel to the direction of rise is 170 MPa to 340 MPa lower than in case of loading  
153 perpendicular to the direction of rise.

### 154 **2.1.2 Uniaxial compression tests on small AAC walls**

155 The performed experimental campaign has also included 7 compression tests on  
156 small AAC walls, having the same loaded area as the blocks previously described  
157 (625 x 100 mm), but a greater height (750 mm, Fig. 3). These compression tests on  
158 small walls have been carried out at the same time as the ones on blocks; as a  
159 consequence, the same experimental apparatus has been adopted (Fig. 3b).

160 As can be seen from Figure 4a, the mean value of compressive strength measured  
161 on small walls was very similar to that determined on blocks; in this case, the obtained  
162 results were even characterized by a lower scatter (with a coefficient of variation  $CV$   
163 equal to 7% instead of 14%). The average value of ultimate load was indeed  
164 approximately equal to  $P_c = 148.8$  kN, corresponding to a nominal compressive strength  
165  $f_c = 2.39$  MPa. This seems to suggest that specimen geometry exerts only a limited  
166 influence on nominal compressive strength. Moreover, the failure mode and the  
167 corresponding crack pattern of small walls were very similar to the ones already  
168 observed for blocks, since also in this case specimen failure was characterized by a  
169 widespread cracking, mainly concentrated near one of the external corners (Fig. 4b).  
170 Finally, it can be observed that the elastic modulus, as well as the Poisson coefficient  
171 indirectly determined on small walls slightly deviates from those already derived from  
172 blocks, being respectively equal to  $E = 1352$  MPa and  $\nu = 0.38$ , with a coefficient of  
173 variation approximately equal to 4%. In this case, Equation 1 provides a value of the  
174 elastic modulus equal to  $E = 1497$  MPa, which is about 10% higher than the measured  
175 one.

176

### 177 **2.1.3 Uniaxial compression tests on AAC cubes and prisms**

178 Finally, the compressive strength values obtained on blocks and small walls have  
179 been compared with those obtained on standard cubes with an edge length of 100 mm  
180 [15]. These compression tests have been performed according to UNI EN 772-1 [16]  
181 and UNI EN 771-4 [17], by cutting the cubes from AAC bearing masonry blocks  
182 (whose dimensions were 625 x 250 x 300 mm), characterized by a moisture content  
183 approximately equal to 6% (and then comparable to that of specimens described in the  
184 previous paragraphs). The so obtained results are summarized in Figures 5a,b which

185 report the trend of compressive strength values respectively in the vertical – parallel to  
186 the applied load – and horizontal directions (lilac histogram, C1-C6 and C1\*-C6\*  
187 samples). On this point, it should be underlined that each reported value has been  
188 deduced as the average between the strength of three specimens, respectively cut in the  
189 upper, the middle and the lower third of each block (as a consequence, a total amount of  
190 18 specimens have been analyzed in the two directions of load). This has permitted to  
191 take into account the effect of density variation along the block. As can be seen, a  
192 different direction of load application determines different average strengths (which are  
193 about 25% higher in the direction of vertical loads), since they are influenced by the  
194 direction of mass expansion during manufacture.

195 The same graph of Figure 5a also reports the strengths of two more cubes (red  
196 bars, C7-C8 samples), which have been directly cut from the central part of block B1 at  
197 the end of compression tests described in §2.1.1. The so obtained cube strength values  
198 appear to be slightly lower than those obtained from C1-C6 samples, even if the  
199 moisture content and effective density were almost the same. In any case, the average  
200 cube compressive strength in the direction of vertical load appears to be up to 25%  
201 higher than the corresponding one measured on slender blocks if all the specimens of  
202 Figure 5a are considered, while it is about 15% higher if only the two cubes cut from  
203 block B1 are considered (red bars).

204 Furthermore, 3 prisms with 40 mm square basis and an height of 80 mm extracted  
205 from the same batch of blocks B1-B13 have been tested in compression; also in this  
206 case, the specimens have been directly cut from the central part of the blocks. As can be  
207 observed from Figure 6a, strength measured on prisms (characterized by a slenderness  
208 equal to 2) results about 10% lower than that determined on cubes, as could be  
209 expected. In order to obtain the stress-strain curve for AAC in compression, these tests  
210 have been performed under displacement control. Longitudinal strains have been  
211 experimentally measured by means of 4 LVDTs placed on the 4 edges of each prism.  
212 The obtained results have been reported in Figure 6b; for comparison, the same graph  
213 also shows the stress-strain curve published in [10] for AAC cylinders with a similar  
214 density (respectively equal to 544 kg/m<sup>3</sup> for AAC1 and 450 kg/m<sup>3</sup> for AAC2). As can  
215 be seen, Figure 6b confirms a good agreement between the curves of the two  
216 experimental campaigns.

217 Finally, the obtained results have been summarized in Figure 6c in terms of  
218 compressive strength values relative to different geometries and dimensions of the  
219 investigated samples. As can be expected, compressive strength determined on prisms is  
220 slightly lower than that obtained from standard cubes, being  $f_c = 2.8$  MPa instead of  
221 3.1 MPa (with a  $CV$  respectively equal to 5% and 7%). Compression tests on blocks and  
222 reduced scale walls provide instead almost the same value of compressive strength  
223 (around  $f_c = 2.4$  MPa), which is about 20% lower than the value obtained from standard  
224 cubes.

225

## 226 ***2.2 Evaluation of AAC tensile strength through three-point bending tests***

227 In order to evaluate AAC tensile strength and its statistical variability, a  
228 preliminary set of three-point bending tests have been carried out on 6 AAC beams  
229 having the same geometry as the blocks tested in compression (625 x 100 x 250 mm).  
230 Moreover, 7 additional three-point tests have been also performed on AAC deep-beams,  
231 having the same geometry as the small walls tested in compression  
232 (625 x 100 x 750 mm). Before testing, all the considered specimens have been  
233 preliminary cured in laboratory conditions for about three months, until the reaching of  
234 moisture content lower than 10%. Tests have been carried out at the Material and  
235 Testing Laboratory of the AAC Manufacturer Company (in Piacenza, Italy), by using a  
236 Instron 5882 press working under loading control, with a loading rate of 1 kN/min [13].  
237 The test setup is shown in Figure 7. Two specimens of each considered typology (beams  
238 and deep-beams) have been instrumented with LVDTs, in order to measure horizontal  
239 displacements at their top and bottom edges (Fig. 7a). In case of deep-beams, an  
240 additional LVDT has been placed in the central part of specimen side (Fig. 7c). Through  
241 these tests it has been possible to determine the failure load in bending for the two  
242 examined types of specimens. Subsequently, the flexural tensile strength  $f_{ct,fl}$  (also called  
243 modulus of rupture) has been indirectly derived from linear finite element analyses.  
244 More in details, the performed experimental tests have been numerically modeled by  
245 adopting the mechanical properties previously derived from the compression tests, by  
246 considering average values between beams and deep-beams ( $E = 1320$  MPa,  $\nu = 0.38$   
247 MPa). The small difference of elastic moduli in the two directions (parallel and

248 perpendicular to the applied load, [14]) has been instead neglected for sake of  
249 simplicity.

250

### 251 **2.2.1 Three-point bending tests on AAC beams**

252 Three-point bending tests on AAC beams have highlighted a small variability of  
253 the failure load in flexure. After the reaching of the peak load, all the specimens were  
254 characterized by a brittle failure, with the development of a main crack placed nearly at  
255 midspan (Fig. 7b). The mean value of flexural tensile strength, determined through a  
256 linear elastic FE inverse analysis, was approximately equal to  $f_{ct,fl} = 0.6 \text{ N/mm}^2$ , with a  
257 coefficient of variation  $CV$  of about 7% (Fig. 8a). This value fits quite well the design  
258 provisions suggested in [14], where the flexural tensile strength  $f_{ct,fl}$  is related to the  
259 compressive strength  $f_c$  through the expression:

$$260 \quad f_{ct,fl} = 4.8 (f_c)^{0.5}, \quad (2)$$

261 with  $f_{ct,fl}$  and  $f_c$  in psi. By substituting the compressive strength determined on blocks  
262 ( $f_c = 2.43 \text{ MPa}$ ) in this latter equation, a value of  $f_{ct,fl} = 0.62 \text{ MPa}$  can be obtained, which  
263 is very similar to the one provided by FE inverse analysis. RILEM provisions [3]  
264 suggests instead the following relation between the flexural tensile strength  $f_{ct,fl}$  and  
265 compressive strength  $f_c$ :

$$266 \quad f_{ct,fl} = 0.27 + 0.21 f_c, \quad (3)$$

267 so providing an higher and in some cases unconservative [14] value of flexural tensile  
268 strength (for the considered case,  $f_{ct,fl} = 0.78 \text{ MPa}$ ). In any case it should be remarked  
269 that AAC is slightly stronger in flexural tension if flexural stresses are oriented parallel  
270 (rather than perpendicular) to the direction of rise [14].

271

### 272 **2.2.2 Three-point tests on AAC deep-beams**

273 The results obtained from three-point tests on AAC deep-beams have confirmed  
274 the small variability of the flexural failure load. Also in this case, specimens showed a  
275 brittle failure, characterized by the spreading of an inclined main crack, starting from  
276 the bottom of the specimen, at a distance approximately ranging from 80 to 150 mm

277 (105 mm on average) from its external edge (Fig. 7d). As regards flexural tensile  
278 strength, a mean value of  $f_{ct,fl} = 0.76 \text{ N/mm}^2$  – quite similar to that determined on AAC  
279 beams – with a coefficient of variation  $CV$  of about 9%, has been deduced from linear  
280 elastic FE modeling (Fig. 8b). It should be observed that Equations 2 and 3 provide the  
281 same results already obtained for beams, due to the similar values of compressive  
282 strength (see §§ 2.1.1 and 2.1.2).

283

### 284 **3. COHESIVE MODEL AND FRACTURE ENERGY**

#### 285 **3.1 Experimental evaluation of AAC fracture energy**

286 As already mentioned, some three-point bending tests on AAC beams have been  
287 also repeated under crack-mouth opening displacement ( $CMOD$ ) control, so as to obtain  
288 the fracture energy  $G_F$  and calibrate a proper cohesive law for the investigated material.  
289 These tests have been carried out at the Materials and Structures Laboratory of Milan  
290 Polytechnic University, by using an INSTRON 8862 universal testing machine,  
291 working under  $CMOD$  control with a speed of  $1 \mu\text{m}/\text{min}$ . The effective geometry of the  
292 three considered specimens is depicted in Figure 9a; as can be observed, a notch has  
293 been made in the central part of the bottom edge, so as to guide the crack location. A  
294 clip gauge has been fixed to the mouth of the notch, in order to control and measure the  
295 crack opening  $w$  during the tests (Figure 9b). Moreover, deflection  $\delta$  has been measured  
296 through a LVDT transducer applied on a specific device fixed onto supports; at the  
297 same time, also the press displacement  $\delta_s$  has been recorded. More details about  
298 specimen geometry and notch dimensions are reported in Table 1.

299 In order to observe the cracking onset and propagation, an ESPI measurement  
300 system [18] has been used. This system adopts a 20 mW Helium-Neon (HeNe) laser,  
301 which operates at a wavelength of  $\lambda = 632.8 \text{ nm}$  in the red part of the visible spectrum.  
302 The adopted optical setup, which has been mounted to observe horizontal  
303 displacements, is showed in Figure 10. As can be seen, the ray generated by the light  
304 source is splitted into two identical beams by a beam-splitter. Each of these beams is  
305 deviated through mirrors along a different path and hits the specimen surface with the  
306 same incidence angle with respect to its normal (Figure 10a). Passing through  $40\times$

307 microscope lens, the light beams are converted into spherical waves, which reach the  
308 specimen surface illuminating a circular area with 150 mm diameter. The mutual  
309 interference of these wave fronts creates a dotted pattern, called speckle, on the  
310 illuminated surface. When the specimen undergoes a deformation the illuminated  
311 surface changes, and consequently also the speckle pattern varies. The resulting images  
312 are recorded by a CCD camera and digitally acquired through an image processing  
313 system with frame grabber interface. Then, the fringe patterns are obtained as the  
314 difference (in terms of pixel intensity values) between the current image and the initial  
315 reference image. These fringes can be regarded as contour lines representing the  
316 incremental displacement of the illuminated surface with respect to the reference image  
317 (Figure 11), with an accuracy greater than 0.1  $\mu\text{m}$ . However, the deduction of  
318 displacement field from the fringe pattern is not straightforward, since it requires to  
319 count the full fringes (representing the locus of points characterized by the same  
320 displacements) of each image and multiply them for a coefficient depending on the  
321 ESPI setup. Automatic methods for this procedure, called unwrapping, could be  
322 otherwise performed [19]. Anyway, in this work ESPI images have been qualitatively  
323 read so as to determine cracking onset and crack depth  $h_w$ , while crack width  $w$  has been  
324 deduced just on the basis of clip-gauge measurements.

325         Figures 11a-c report the experimental curves obtained for the three investigated  
326 AAC beams in terms of load  $P$  vs. midspan deflection  $\delta$  and the ESPI images  
327 corresponding to the attainment of cracking and peak loads (respectively indicated as  
328  $P_{cr}$  and  $P_u$ ). On the same Figures the crack depth  $h_w$  at peak, as deduced from ESPI  
329 images, as well as the measured fracture energy  $G_F$  are also indicated for each  
330 specimen. More in details, fracture energy has been determined as the total work of  
331 fracture  $W$ , given by the area under the complete load  $P$  - displacement  $\delta$  curve, divided  
332 by the ligament area; the work done by the self weight has been properly subtracted. As  
333 can be seen, while the results of the first two tests (BB1 and BB2) are similar to each  
334 others, also in terms of fracture energy (approximately equal to 4.7 N/m), those  
335 obtained from the third specimen BB3 are instead anomalous, since the softening  
336 branch is less steep, so providing an almost double value of the fracture energy.  
337

338 **3.2 Calibration of a proper cohesive law through inverse XFEM analysis**

339 The so obtained results have been subsequently numerically elaborated so as to  
340 calibrate a proper cohesive law suitable for the investigated material, by performing an  
341 inverse extended finite element (XFEM) analysis.

342 The extended finite element method has been here preferred since it eases the  
343 difficulties in solving problems with localized features (e.g., the presence of a main  
344 crack) that are not efficiently resolved by mesh refinement. XFEM represents indeed an  
345 extension of the conventional FE method based on the concept of partition of unity [20],  
346 which takes into account a priori the discontinuous structure of the displacement field  
347 [21, 22]. Enrichment functions connected to additional degrees of freedom are added to  
348 the finite element approximation in the region of the mesh where the crack is located.  
349 These enrichment functions usually consist of the asymptotic crack tip functions that  
350 capture the singularity at the crack tip and a discontinuous function that represents the  
351 gap between the crack surfaces [e.g., 23-25]. A key advantage of this procedure is that  
352 the finite element mesh does not need to be updated to track the crack path, providing at  
353 the same time a good approximation of the displacements and, generally, leading to  
354 symmetric stiffness matrices. Since its introduction, XFEM has been subjected to  
355 different developments and improvements. As an example, in the last ten years it has  
356 been combined with cohesive crack models so allowing the simulation of fracture in  
357 quasi-brittle heterogeneous materials [26, 27]. Other developments have regarded the  
358 simulation of crack propagation in composite materials [28] and the combination of  
359 XFEM with other techniques so as to increase the rate of convergence (e.g., cut off  
360 functions and geometric enrichment, [29, 30]). Moreover, several researches have been  
361 devoted to the solution of numerical and technical problems, mainly related to  
362 enrichment implementation, as well as to the assembly of the stiffness matrix (which  
363 requires integration of singular/discontinuous functions) and to the quadrature of the  
364 weak form (among others, e.g., [31-34]). Traditional quadrature techniques, which are  
365 successfully adopted for standard finite elements, should be indeed modified when the  
366 approximation space is enriched by singular/discontinuous functions, since inaccurate  
367 quadrature can lead to poor convergence and inaccuracy in the solution.

368 Besides current research developments, standard XFEM is currently available in

369 widely diffused general purpose codes, as the one (ABAQUS, [35]) used in this work to  
370 perform numerical simulations.

371 In this paper standard XFEM inverse analyses have been first performed on AAC  
372 beams, so as to study crack propagation (experimentally observed through ESPI  
373 technique), as well as to calibrate a proper cohesive law for the material. To this scope,  
374 according to Figure 9a and Table 1 (which are relative to experimental samples), an  
375 AAC beam with nominal dimensions equal to 620 x 100 x 250 mm has been modelled,  
376 with a 15 mm deep central notch. The presence of the notch has been accounted in  
377 numerical modeling by inserting a seam crack with the same dimensions and in the  
378 same position as the notch itself (a seam defines an edge in the model that is originally  
379 closed but can open during the analysis, due to the presence of overlapping duplicate  
380 nodes).

381 The beam has been discretized with 4 nodes plane stress elements with reduced  
382 integration (CPS4R in the adopted FE code library). A structured mesh has been  
383 adopted, by using 2.5 mm side square elements. To simulate the interaction between the  
384 AAC beam and the supporting steel plates, as well as between the plates and the steel  
385 rollers, an interface law has been defined, based on the measured friction coefficients  
386 (which have been set respectively equal to 0.7 for the steel-steel interface and 0.3 for the  
387 steel-AAC interface). AAC has been treated as a linear elastic material both in the  
388 tension and compression regime, by assuming the same values of elastic modulus  $E$  and  
389 Poisson coefficient  $\nu$  already described in § 2.2 ( $E = 1320$  MPa,  $\nu = 0.38$  MPa).  
390 Mechanical nonlinearities have been taken into account through the XFEM-based  
391 cohesive segments method [27], which allows to model cracking growth along an  
392 arbitrary, solution-dependent path in the material (crack position is indeed not tied to  
393 the element boundaries in the mesh). The discontinuity of the cracked elements is  
394 represented by introducing phantom nodes, which are superposed on the original real  
395 nodes [35]. When the element is intact, each phantom node is completely constrained to  
396 its corresponding real node; otherwise, when the element is cut through by a crack, the  
397 cracked element splits into two parts. Each phantom node and its corresponding real  
398 node are no longer tied together and can move apart. The magnitude of the separation is  
399 governed by the cohesive law until the cohesive strength of the cracked element is zero,  
400 after which the phantom and the real nodes move independently.

401 The behavior of XFEM-based cohesive segments for a crack propagation analysis  
 402 is governed by the traction-separation model available in ABAQUS [35], which  
 403 assumes an initially linear elastic behavior followed by the initiation and evolution of  
 404 damage. More in details, when stresses or strains satisfy specified crack initiation  
 405 criteria, the cohesive response at an enriched element begins to degrade, so determining  
 406 crack initiation. In this work, the crack initiation criterion based on the maximum  
 407 principal stress has been chosen, and consequently the process of degradation is  
 408 assumed to start when the maximum principal stress attains the direct tensile strength of  
 409 AAC. Subsequently, crack propagation is handled through a damage evolution law  
 410 describing the rate at which the cohesive stiffness is degraded during the analysis.

411 In the performed numerical analysis, the direct tensile strength of AAC has been  
 412 set equal to  $f_{ct} = 0.54$  MPa, in order to correctly represent the mean value of the  
 413 cracking load  $P_{cr}$  registered during the three tests (reported in Fig. 11a-c). As can be  
 414 seen, this value of direct tensile strength  $f_{ct}$  is approximately equal to  $0.9 f_{ct,fl}$ , being  $f_{ct,fl}$   
 415 the flexural tensile strength provided by three-point bending tests on beams. For the  
 416 cohesive law, an exponential relation has been chosen, having the form:

$$417 \quad \sigma = [1 - d(w)] \cdot f_{ct} \quad (4)$$

418 where  $\sigma$  is the cohesive stress,  $f_{ct}$  the direct tensile strength of AAC and  $d$  is a damage  
 419 parameter having the form:

$$420 \quad d(w) = \frac{1 - e^{-\alpha \frac{w}{w_u}}}{1 - e^{-\alpha}} \quad (5)$$

421 being  $w_u$  the failure displacement, set equal to 0.08 mm, and  $\alpha = 5$  an exponential  
 422 parameter. These latter variables have been calibrated so as to obtain the mean  
 423 experimental value of fracture energy  $G_F$  (Figs. 11a-c). This exponential law has been  
 424 plotted in Figure 11d, where it is also compared with other bilinear strain-softening  
 425 relations for AAC based on experimental wedge-splitting tests (on specimens  
 426 characterized by an average density of about  $400 \text{ kg/m}^3$ ), available in the literature [4].

427 In order to trace the softening branch, the numerical analysis has been performed  
 428 by adopting the Riks method [36]. The comparison between the so obtained numerical  
 429 curve and the experimental ones is reported in Figure 12a, in terms of applied load  $P$  vs.

430 crack mouth opening displacement  $CMOD$ . As can be seen, the good agreement  
431 between calculated and experimental responses suggests that the adopted exponential  
432 law is able to realistically describe crack formation and propagation in AAC. Finally,  
433 Figure 12b shows a comparison between experimental and numerical crack pattern at  
434 peak load (point A in Fig. 12a). More in details, the ESPI image has been compared to  
435 the crack pattern provided by the extended finite element analysis in terms of the  
436 variable STATUSXFEM, representing the status of each enriched element in the mesh.  
437 In particular, this variable is equal to 1 if the element is completely cracked, 0 if the  
438 element contains no crack and it is variable between 1 and 0 if the element is partially  
439 cracked. As can be seen, the adopted XFEM procedure is able to correctly represent  
440 crack propagation into the AAC matrix, also providing a good estimate of crack depth  
441  $h_w$ .

442

#### 443 **4. AAC DEEP-BEAMS BEHAVIOR: EXPERIMENTAL TEST AND**

#### 444 **NUMERICAL MODELING BY XFEM**

445 In order to further validate the proposed approach, an additional three-point test  
446 has been carried out under  $CMOD$  control on an AAC deep-beam; also in this case, the  
447 ESPI setup has been used so as to observe cracking onset and propagation. Figure 13a  
448 shows the effective geometry of the considered specimen, characterized by the presence  
449 of a notch in the central part of its bottom edge; this permits a symmetric behavior  
450 avoiding mixed mode cracking complications. The adopted test instrumentation is the  
451 same already described in the previous paragraph for beams. The obtained experimental  
452 curve is reported in Figure 13b in terms of applied load  $P$  vs. midspan deflection  $\delta$ ; the  
453 same Figure also shows the ESPI images corresponding to the cracking load  $P_{cr}$ , as well  
454 as to a load equal to 15.6 kN, at which the crack tip exits from the visual field.  
455 Consequently, in this case it has not been possible to measure the crack depth  
456 corresponding to the peak load  $P_u$ .

457 This experimental test has been subsequently modeled by XFEM, by following  
458 the same procedure already described in §3.2. Also in this case a structured mesh  
459 formed by 5 mm side square CPS4R elements has been adopted. AAC mechanical  
460 behavior has been again described through a linear elastic law (assuming  $E = 1320$  MPa

461 and  $\nu = 0.38$ , as for beams), coupled to the XFEM-based cohesive segments method for  
462 the modeling of cracking growth. The adopted direct tensile strength, as well as the  
463 cohesive law is the same as determined on beams (see §3.2). It should be remarked that  
464 in this case the schematization of boundary conditions is slightly different from that  
465 described for beams, since the horizontal translation of the roller was partially prevented  
466 during the test, so determining the appearance of an arch effect and an increase in the  
467 experimental peak load. In order to correctly catch these aspects, the roller has been  
468 constrained with a non-linear spring, whose stiffness has been properly calibrated on the  
469 basis of the experimental behavior of the support. The interaction between the AAC  
470 specimen and the steel plates and between these latter and the rollers has been instead  
471 schematized through the same interface laws already adopted for the beam. The analysis  
472 has been carried out under load control.

473 The obtained results are depicted in Figure 14a, in terms of applied load  $P$  vs.  
474 crack mouth opening displacement  $CMOD$ . As can be observed, the proposed approach  
475 allows providing a correct estimate of the peak value, even if the numerical model is not  
476 able to catch the softening branch, which is very steep. The obtained numerical crack  
477 pattern at peak is reported in Figure 14b, through the STATUSXFEM variable. Other  
478 comparisons between experimental and numerical results are shown in Figure 15 in  
479 terms of crack pattern at an applied load  $P = 15.5$  kN (as already mentioned, for higher  
480 loads the crack tip exits from the ESPI visual field), highlighting the capability of the  
481 performed simulation to represent crack propagation. Results seem to confirm that the  
482 proposed cohesive law combined with an XFEM procedure can represent a useful tool  
483 for the modeling of cracking development in AAC walls.

484

## 485 **5. CONCLUSIONS**

486 The present work aims to investigate and model cracking development in AAC  
487 beams and deep-beams. First, the problem has been experimentally afforded, by  
488 carrying out a series of tests devoted to material characterization both in compression  
489 and in flexure (through the execution of three-point bending tests), taking into account  
490 the effect of different shapes and dimensions of the investigated samples. The so  
491 obtained results have been subsequently adopted in extended finite element analyses, in

492 order to calibrate a proper cohesive law for AAC, suitable for the modeling of cracking  
493 onset and propagation in infill and bearing walls under static loads. The main  
494 conclusions of this work can be so summarized:  
495 - being equal the material density and the moisture content, the statistical variability of  
496 AAC mechanical properties (compressive and tensile strengths, elastic modulus and  
497 Poisson coefficient) is rather limited (below 10%); furthermore, even changing the  
498 shape and dimensions of tested samples, the obtained values have a quite limited scatter  
499 (e.g., compressive strength of small walls is about 20% lower than that measured on  
500 standard cubes). This implies that the mechanical properties measured on standard  
501 specimens are quite representative of the behavior of full-scale walls (a correction factor  
502 should be probably introduced in some cases), as well as of the behavior of non  
503 standard specimens which can be extracted from existing buildings (these latter, in  
504 general, may be indeed different in shape and dimensions from standard samples).  
505 - load-displacement curves obtained from three-point bending tests under *CMOD*  
506 control on AAC beams show a limited scatter and provide a value of the fracture energy  
507  $G_F$  almost equal to 5-6 N/m, which is quite similar to other results obtained in the  
508 technical literature by means of wedge-splitting tests;  
509 - on the basis of the experimental results, an exponential cohesive law has been  
510 calibrated through inverse extended finite element analysis. This law has subsequently  
511 been applied in the simulation of a three-point test on a AAC deep-beam, whose  
512 behavior is more similar to full scale infill panels.

513 The proposed model appears to be able to correctly catch both the peak load and  
514 the experimental crack pattern development, as revealed by the comparison with ESPI  
515 images. The obtained cohesive law can be then applied for the analysis of full scale walls,  
516 in order to study cracking development under static loads, which is a quite common  
517 problem in residential buildings.

518 .

## 519 **ACKNOWLEDGEMENTS**

520 Mr. Matteo Riva is gratefully acknowledged for his contribution in the execution of  
521 experimental tests in Piacenza. The Authors would also sincerely thank Prof. Ivo Iori  
522 for his scientific support and motivation in this research.

523

524

525

526 **REFERENCES**

- 527 [1] Limbachiya MC, Roberts JJ Eds. Proc. 4<sup>th</sup> Int Conf on AAC - Autoclaved Aerated  
528 Concrete: innovation and development. Taylor & Francis, London, 2005.
- 529 [2] Wittmann FH Eds. Proc. 3<sup>rd</sup> RILEM Int Symp on AAC - Advances in Autoclaved  
530 Aerated Concrete. Balkema, Rotterdam, 1992.
- 531 [3] Aroni S, De Groot GJ, Robinson MJ, Svanholm G, Wittmann FH Eds. Autoclaved  
532 aerated concrete: properties, testing and design. RILEM Recommended Practice.  
533 E&FN Spon, London, 1993.
- 534 [4] Trunk B, Schober G, Helbling AK, Wittmann FH. Fracture mechanics of autoclaved  
535 aerated concrete. Cem Concr Res 1999; 29: 855-859.
- 536 [5] Brühwiler E, Wang J, Wittmann FH. Fracture of AAC as influenced by specimen  
537 dimension and moisture. J Mat Civ Eng 1990; 2: 136-146.
- 538 [6] Wittmann FH, Gheorghita I. Fracture toughness of autoclaved aerated concrete. Cem  
539 Concr Res 1984; 14:369-374.
- 540 [7] Isu N, Teramura S, Tshida H, MitsudaT. Influence of quartz particle size on the  
541 chemical and mechanical properties of autoclaved aerated concrete (II): fracture  
542 toughness, strength and micropore. Cem Concr Res 1995; 25: 249-254.
- 543 [8] Narayanan N, Ramamurthy K. Structure and properties of aerated concrete: a  
544 review. Cem & Concr Comp 2000; 22:321-329.
- 545 [9] Valore RC. Cellular concretes - Part 2: Physical properties. J American Concr Inst  
546 1954; 50: 817-836.
- 547 [10] Marzahn GA. Extended investigation of mechanical properties of masonry units.  
548 LACER No. 7, 2002: 237-254.
- 549 [11] Tanner JE. Design provisions for autoclaved aerated concrete (AAC) structural  
550 systems. PhD Thesis, University of Austin, Texas, 2003.
- 551 [12] Wolf S, Wiegand S, Stoyan D, Walther HB. The compressive strength of AAC – a  
552 statistical investigation. Proc. 4<sup>th</sup> Int Conf on Autoclaved Aerated Concrete:  
553 innovation and Development. Taylor & Francis, London, 2005: 287-295.
- 554 [13] Ferretti D, Michelini E, Gazzola G, Riva M, Rosati G. Cracking in AAC elements:  
555 experimental investigation with ESPI technique (in Italian). Proc. 17<sup>th</sup> C.T.E.  
556 Congress, Rome, 2008: 409-417.
- 557 [14] Argudo JF. Evaluation and synthesis of experimental data for autoclaved aerated

558 concrete. PhD Thesis, University of Austin, Texas, 2003.

559 [15] IUAV University. Test Report n°18678 - Determination of AAC mechanical  
560 properties. Venice, 2006.

561 [16] UNI EN 772-1. Methods of test for masonry units - Part 1: Determination of  
562 compressive strength, 2002.

563 [17] UNI EN 771-4. Specification for masonry units - Part 4: Autoclaved aerated  
564 concrete masonry units, 2005.

565 [18] Jones R, Wykes C. Holographic and speckle interferometry. Cambridge University  
566 Press, Cambridge, 1989.

567 [19] Ferretti D, Rossi M, Royer-Carfagni G. An ESPI experimental study on the  
568 phenomenon of fracture in glass. Is it brittle or plastic? *J Mech Phys Solids* 2011;  
569 59(7): 1338-1354.

570 [20] Melenk JM, Babuska I. The partition of unity finite element method: basic theory  
571 and applications. *Comp Meth Appl Mech and Engng* 1996; 39:289–314.

572 [21] Belytschko T, Gracie R, Ventura G. A review of extended/generalized finite  
573 element methods for material modeling. *Model Simul Mater Sci Engng* 2009;  
574 17(4):043001.

575 [22] Richardson CL, Hegemann J, Sifakis E, Hellrung J, Teran JM. An XFEM method  
576 for modeling geometrically elaborate crack propagation in brittle materials. *Int J*  
577 *Numer Meth Engng* 2011; 88: 1042-1065

578 [23] Belytschko T, Black T. Elastic crack growth in finite elements with minimal  
579 remeshing. *Int J Numer Meth Engng* 1999; 45(5): 601-620

580 [24] Moës N, Dolbow J, Belytschko T. A finite element method for crack growth  
581 without remeshing. *Int J Numer Meth Engng* 1999; 46:131–150.

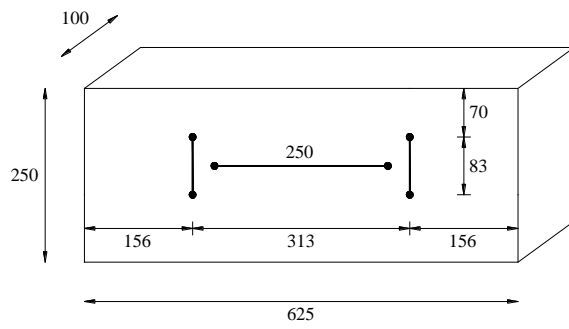
582 [25] Gracie R, Ventura G, Belytschko T. A new fast finite element method for  
583 dislocations based on interior discontinuities. *Int J Numer Meth Engng* 2007;  
584 69:423–441.

585 [26] Moës N, Belytschko T. Extended finite element method for cohesive crack growth.  
586 *Eng Frac Mech* 2002; 69:813–833.

587 [27] Remmers JJC, de Borst R, Needleman A. The simulation of dynamic crack  
588 propagation using the cohesive segments method. *J Mech Phys Solids* 2008, 56: 70–  
589 92.

- 590 [28] Huynh D, Belytschko T. The extended finite element method for fracture in  
591 composite materials. *Int J Numer Meth Engng* 2009; 77(2):214–239.
- 592 [29] Chahine E, Laborde P, Renard Y. Crack tip enrichment in the XFEM using a cutoff  
593 function. *Int J Numer Meth Engng* 2008; 75(6):626–646.
- 594 [30] Lew A, Shen Y. Crack tip enrichment in the XFEM using a cutoff function. *Int J*  
595 *Numer Meth Engng* 2008; 75(6):629–646.
- 596 [31] Ventura G, Gracie R, Belytschko T. Fast integration and weight function blending  
597 in the extended finite element method. *Int J Numer Meth Engng* 2009; 77(1):1–29.
- 598 [32] Benvenuti E, Tralli A, Ventura G. A regularized XFEM model for the transition  
599 from continuous to discontinuous displacements. *Int J Numer Meth Engng* 2008;  
600 74(6):911–944.
- 601 [33] Benvenuti E, Ventura G, Ponara N. Finite element quadrature of regularized  
602 discontinuous and singular level set functions in 3D problems. *Algorithms* 2012; 5:  
603 529-544.
- 604 [34] Benvenuti E, Ventura G, Ponara N, Tralli A. Variationally consistent eXtended FE  
605 model for 3D planar and curved imperfect interfaces. *Comput Methods Appl Mech*  
606 *Engrg* 2013; 267: 434-457.
- 607 [35] ABAQUS 6.12. Online Documentation. Dassault Systèmes Simulia Corp.
- 608 [36] Crisfield M.A. *Nonlinear finite element analysis of solids and structures. Vol. 1:*  
609 *Essentials*. Wiley, New York, 1991.

# FIGURES

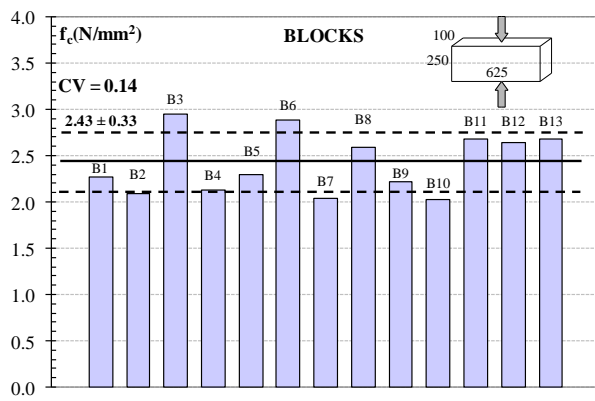


(a)

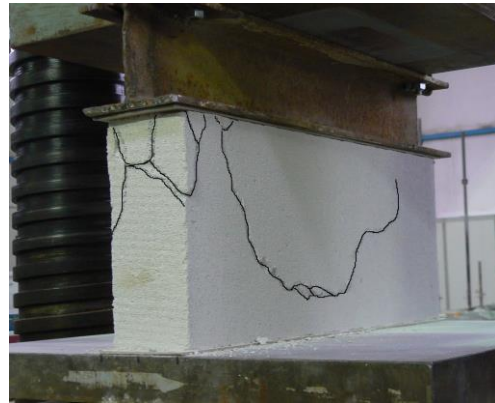


(b)

Figure 1

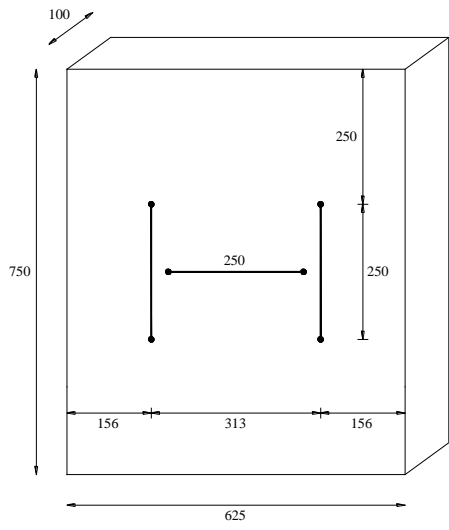


(a)



(b)

Figure 2

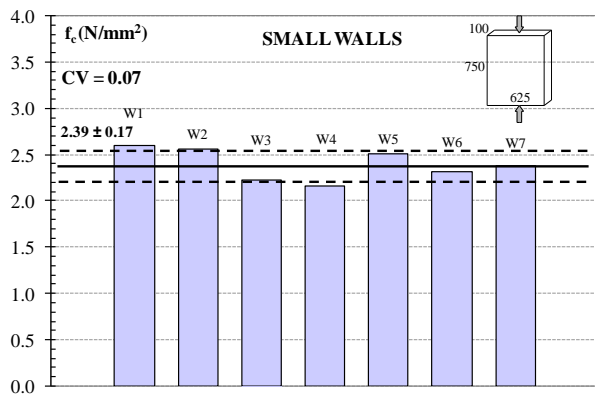


(a)

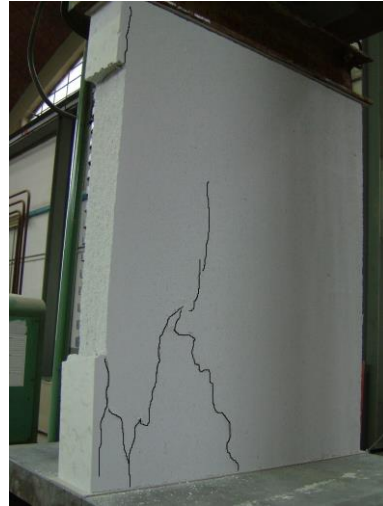


(b)

Figure 3



(a)



(b)

Figure 4

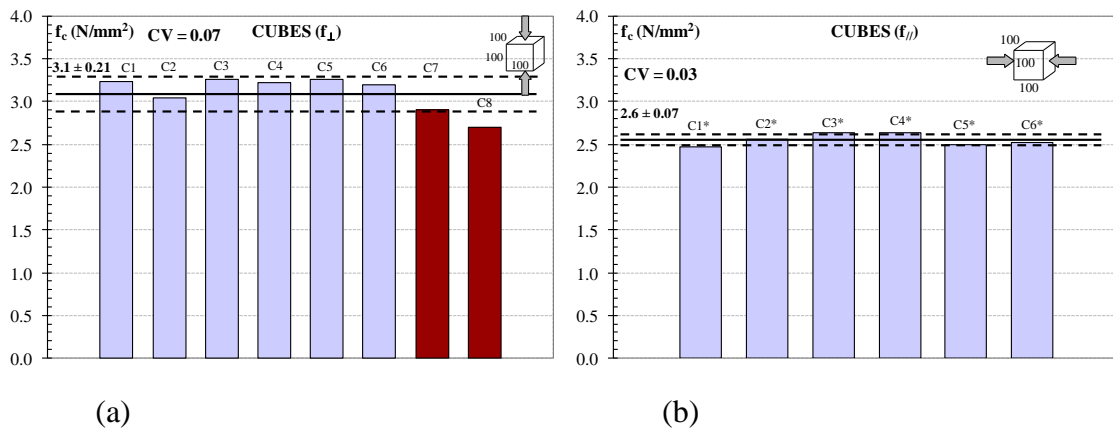


Figure 5

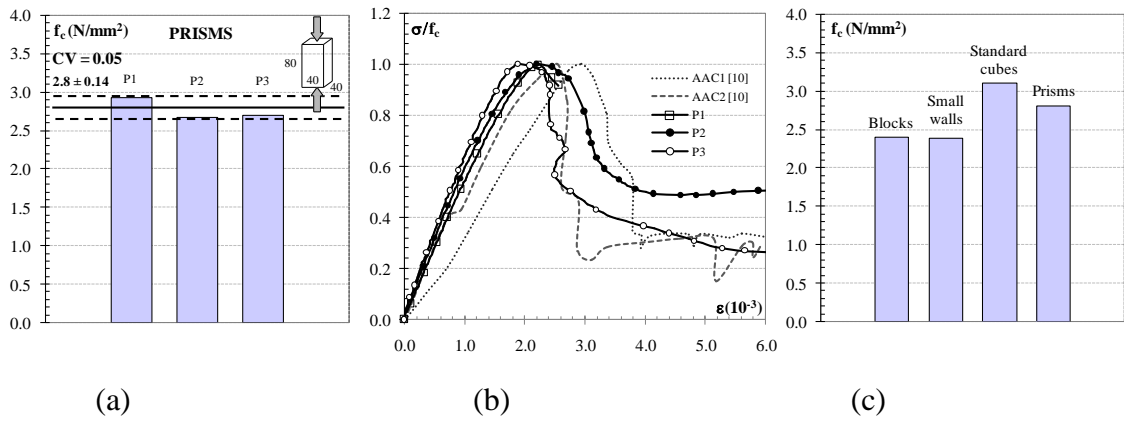
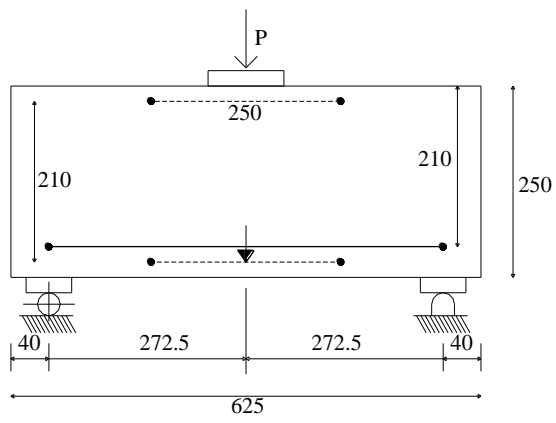
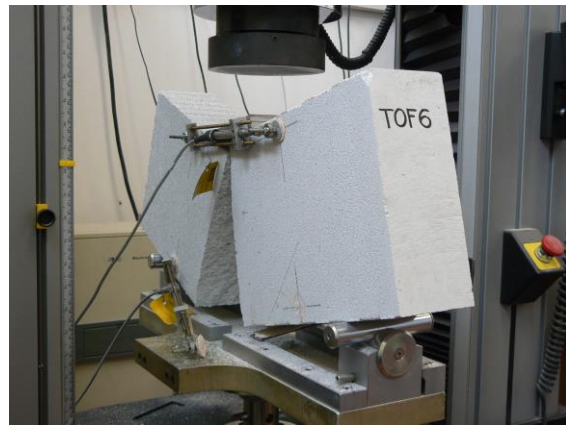


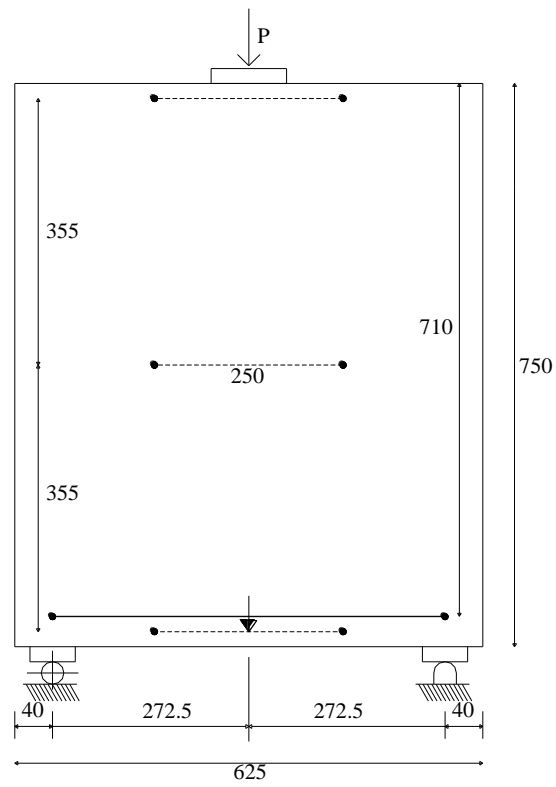
Figure 6



(a)



(b)

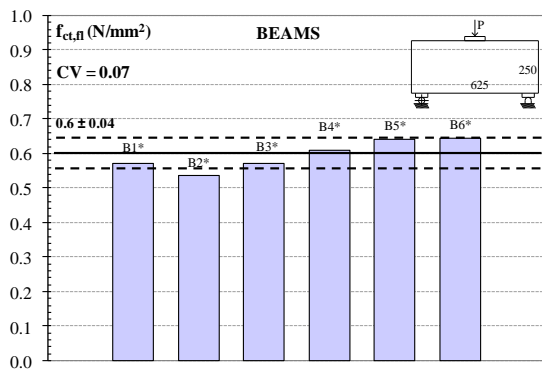


(c)

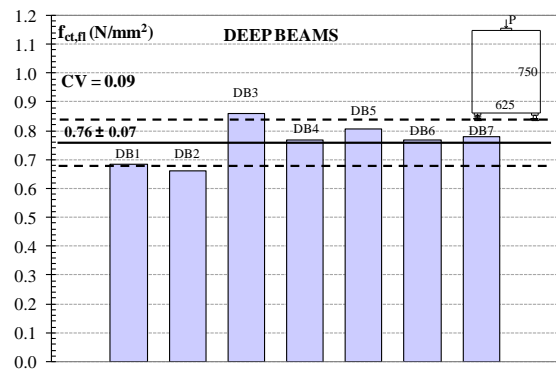


(d)

Figure 7

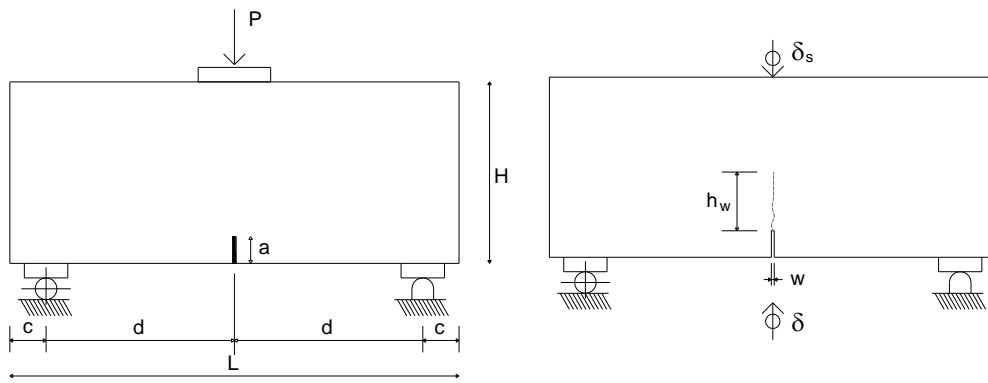


(a)



(b)

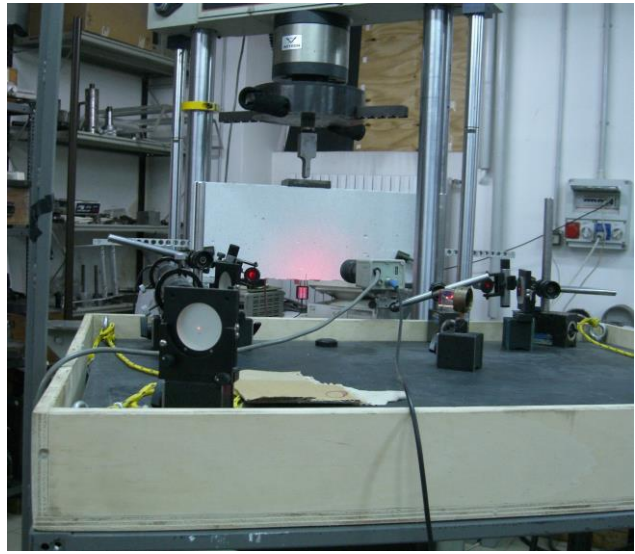
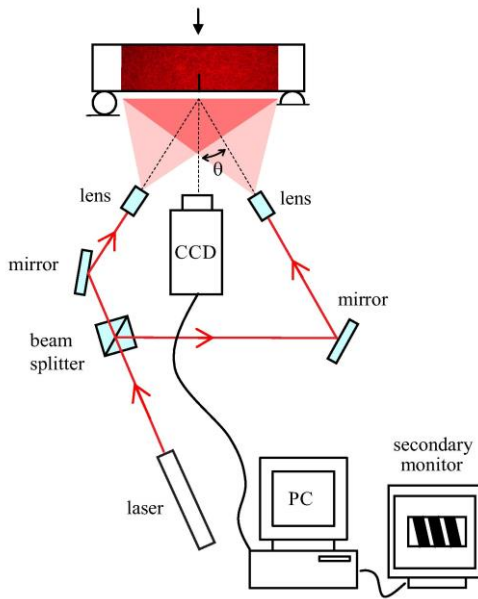
Figure 8



(a)

(b)

Figure 9



(a)

(b)

Figure 10

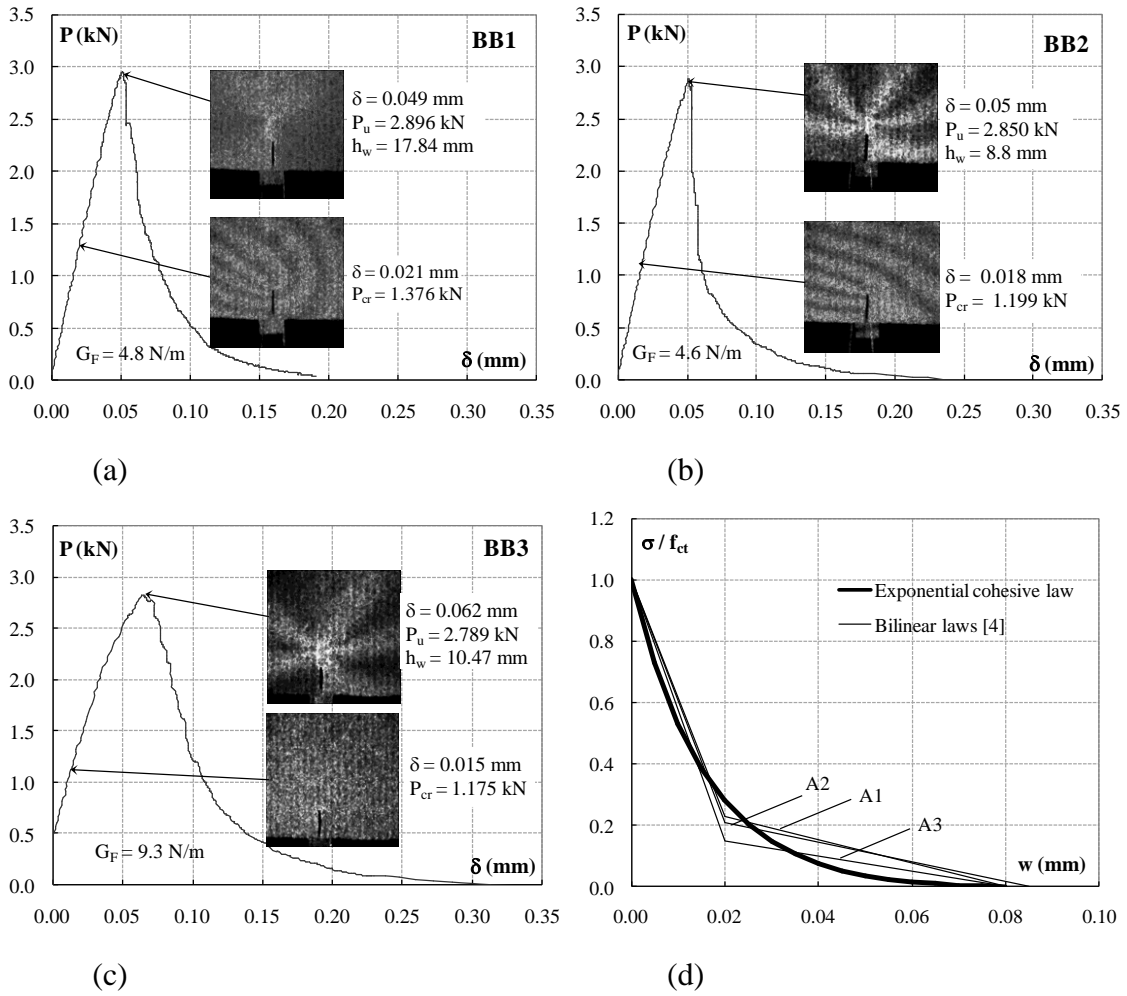
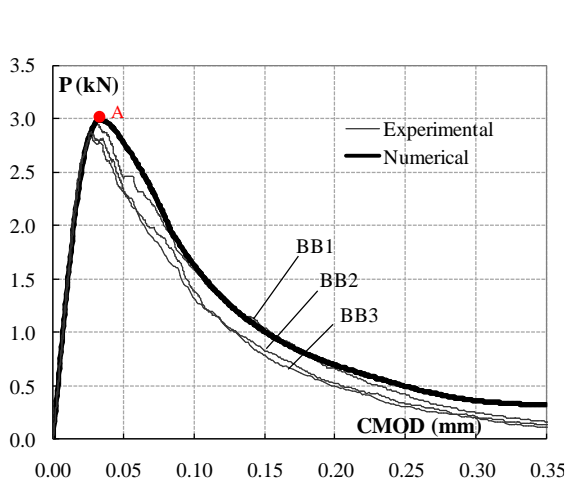
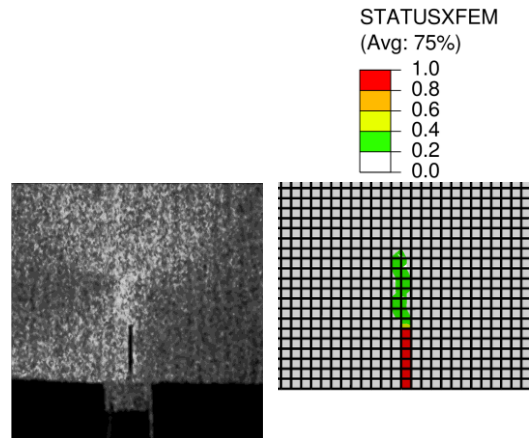


Figure 11

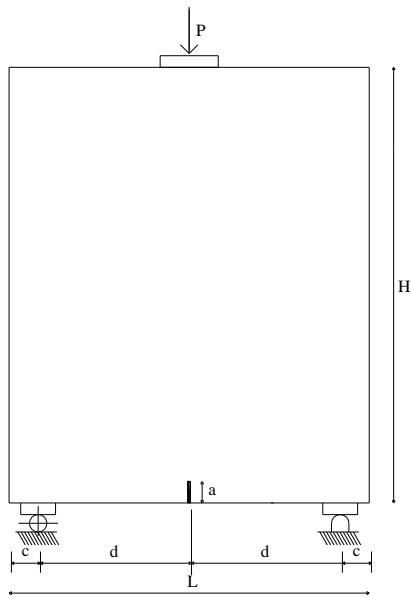


(a)

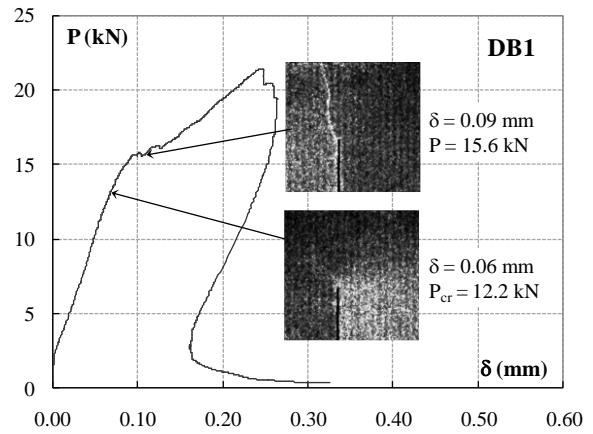


(b)

Figure 12



(a)



Specimen ID	DB1
<b>L x H x b (mm)</b>	624 x 748 x 100
<b>a (mm)</b>	30
<b>c (mm)</b>	40
<b>d (mm)</b>	272

(b)

Figure 13

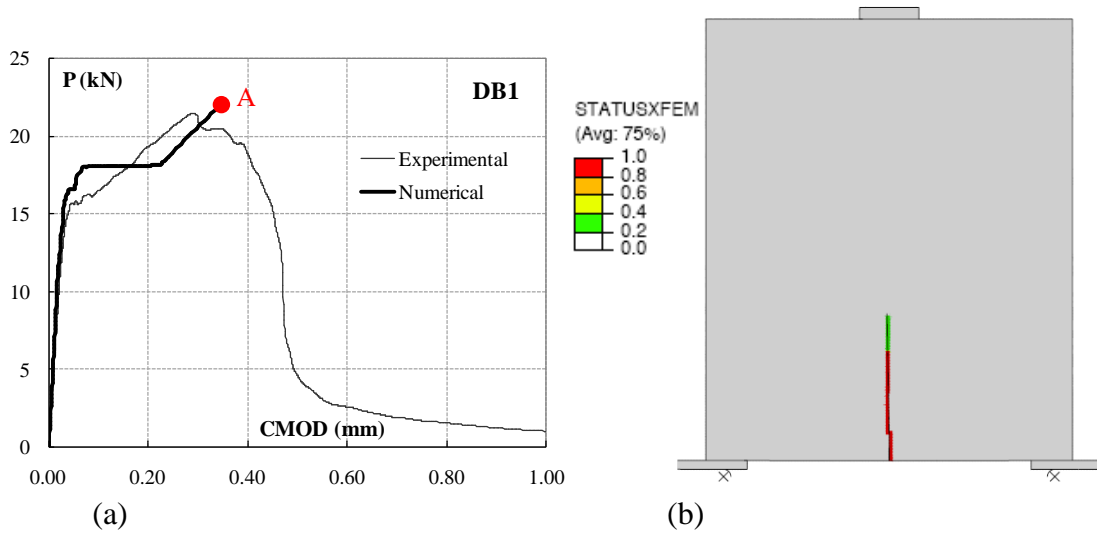


Figure 14

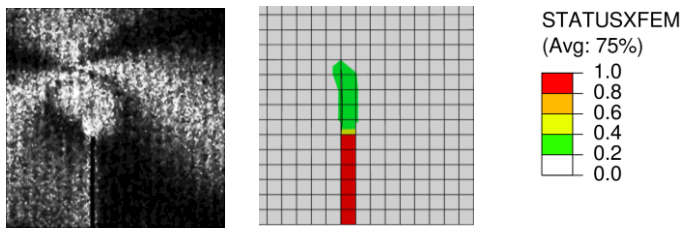


Figure 15

## TABLES

<b>Specimen ID</b>	<b>L x H x b (mm)</b>	<b>a (mm)</b>	<b>c (mm)</b>	<b>d (mm)</b>
BB1	620 x 251.1 x 99.20	14.5	40.0	270.0
BB2	620 x 251.2 x 100.1	12.0	40.0	270.0
BB3	620 x 251.3 x 100.1	12.0	40.0	270.0

Table 1

## LIST OF FIGURES AND TABLES

Figure 1. Compression tests on AAC blocks: (a) geometry of the considered samples with position of the adopted instrumentation; (b) general setup adopted for instrumented tests.

Figure 2. (a) Statistical variability of AAC compressive strength as measured on blocks; (b) example of observed crack pattern at failure.

Figure 3. Compression tests on small AAC walls: (a) geometry of the considered samples with position of the adopted instrumentation; (b) general setup adopted for instrumented tests.

Figure 4. (a) Statistical variability of AAC compressive strength as measured on small walls; (b) example of observed crack pattern at failure.

Figure 5. Statistical variability of AAC compressive strength as measured on cubes with an edge length of 100 mm cut from bearing masonry blocks (in red the ones cut from internal partition blocks), (a) in the direction of vertical loads and (b) in the direction perpendicular to vertical loads, in masonry plane.

Figure 6. (a) Statistical variability of AAC compressive strength as measured on prisms with 40 mm square basis and an height of 80 mm; (b) experimental stress-strain relationship obtained from prisms and comparisons with tests on cylinders in [10]; (c) comparison among different compressive strengths obtained from specimens with different geometries and dimensions.

Figure 7. Geometry of the considered samples with position of the adopted instrumentation for (a) beams and (c) deep-beams; experimental crack pattern at the end of three-point bending tests for (b) beams and (d) deep-beams.

Figure 8. Statistical variability of AAC flexural tensile strength as determined on (a)

beams with 625 mm x 100 mm basis and 250 mm high; (b) deep-beams with 625 mm x 100 mm basis and 750 mm high.

Figure 9. Three-point bending tests on AAC beams under *CMOD* control: (a) specimen geometry and (b) variables measured during the test.

Figure 10. (a) ESPI optical setup; (b) adopted test arrangement.

Figure 11. Experimental load  $P$  - deflection  $\delta$  curves and ESPI images corresponding to cracking load  $P_{cr}$  and peak load  $P_u$  for the three investigated AAC beams: (a) BB1, (b) BB2, (c) BB3; (d) comparison between the adopted exponential cohesive law and relations proposed in [4] for AAC.

Figure 12. AAC beams: (a) comparison between numerical and experimental curves in terms of applied load  $P$  vs. crack mouth opening displacement *CMOD*; (b) comparison between experimental and numerical crack pattern at peak load (point A).

Figure 13. Three-point bending test on a AAC deep-beam under *CMOD* control: (a) specimen geometry and dimensions; (b) experimental load  $P$  - deflection  $\delta$  curve and ESPI images corresponding to cracking load  $P_{cr}$  and to a load  $P = 15.6$  kN.

Figure 14. AAC deep-beam: (a) comparison between numerical and experimental curves in terms of applied load  $P$  vs. crack mouth opening displacement *CMOD*; (b) numerical crack pattern at peak load (point A).

Figure 15. AAC deep-beam: comparison between experimental and numerical crack pattern for an applied load  $P = 15.5$  kN.

Table 1. Effective dimensions of tested specimens and depth of the notch.